Theoretical study of damage accommodation in salt subject to viscous fatigue

C. Zhu & C. Arson
School of Civil and Environmental Engineering
Georgia Institute of Technology, Georgia, USA

A. Pouya
Navier Lab - CERMES, IFSTTAR
Ecole des Ponts Paris Tech, Paris, France

ABSTRACT: Underground salt cavities used for compressed air energy storage undergo cyclic loads and are subject to a fatigue phenomenon that reduces rock strength and stiffness. Understanding such behaviors and developing relevant constitutive models require a micro-mechanical analysis. This study investigates damage and fatigue in salt rock, the extent of which is influenced by its polycrystalline nature, on the basis of self-consistent upscaling approaches for viscous heterogeneous materials. We develop a model that treats monocrystals as spherical inclusions embedded in an infinite homogeneous matrix with purely elastic inclusion-matrix interactions. To predict grain breakage and its subsequent impact, we also introduce a failure criterion. The model provides micro-mechanical interpretations of the common viscoplastic and fatigue behavior of salt such as damage and accelerated creep from grain breakage and the shakedown effect observed in elastoplastic media. Finite element (FE) simulations confirmed the macrostrain and microstress predictions obtained by homogenization. The FE program will be used in future studies to simulate inter-granular fracture propagation. This study provides new perspectives on research pertaining to the microscopic origin of fatigue in viscous polycrystalline materials.

1 INTRODUCTION

Salt cavities used for the underground storage of oil and natural gas sustain weekly to seasonal thermo-mechanical load cycles. Compressed air energy storage (CAES) facilities are subject to shorter load cycles on the order of a day. Experimental data show that the resulting fatigue process of salt rock (i.e., Young's modulus and strength decrease) slows down as the load frequency increases. Fatigue is a significant dimensioning factor for CAES design. However, because of the numerous variables influencing salt damage under cyclic loading (e.g., stress amplitude, loading frequency) and the high number of cycles required to assess the effect of fatigue in the laboratory, the experimental characterization of fatigue in salt rock remains a challenge.

In the present paper, we analyze the origin of salt fatigue from the study of the deformation of micro-mechanisms, which drive the deformation of halite crystals in polycrystalline materials. The plastic and viscous deformation of salt crystals results from several fundamental mechanisms such as dislocation glide, dislocation climb, polygonalization, inter-granular slip, and dissolution-precipitation. Under stress and temperature typical of storage conditions, dislocations are the predominant mechanisms contributing to macroscopic salt rock deformation. Dislocation movements occur only on specific crystallographic surfaces and along a limited number of directions. Restricted movements inside a monocrystalline grain cause incompatibilities between the non-elastic deformation of adjacent grains, which induces internal stresses within the polycrystal.

In this paper, we model the macroscopic viscous behavior of the polycrystalline medium with a self-consistent method. We explain the microscopic origin of fatigue in salt rock in Section 2, present the homogenization scheme in Section 3, and calibrate our micro-macro model of salt viscous fatigue against creep tests reported in the literature in Section 4. Then we simulate both creep tests and cyclic loading tests in Section 5 and present the implementation of the proposed micro-macro evolution law into a finite element method (FEM) based tool, Porofis, in Section 6.

Salt rock subjected to cyclic loads differs greatly from that under static loads in its mechanical properties. As the number of loading cycles increases (Fuenkajorn & Phueakphum 2010, Dubey & Gairola 2000, Ma et al. 2013), Young's modulus and the compressive strength of salt rock decrease. The degradation of elastic moduli increases with maximum stress and with the amplitude of loading (Guo et al. 2012). Fatigue initiates faster for lower loading frequency (Fuenkajorn & Phueakphum 2010, Liang et al. 2011, Ma et al. 2013, Liu et al. 2014). Compared to the amplitude and the frequency, fatigue is not significantly influenced by confining stress (Ma et al. 2013). Dubey & Gairola (2000) also investigated the influence of the orientation of the bedding planes, and Filimonov et al. (2001) analyzed the memory effects in salt subject to triaxial stress states. However, laboratory studies are usually constrained by the range of investigated frequencies, which are significantly higher than those in actual CAES conditions. Because of the requirement of a sufficiently long loading period and a large number of loading cycles, low frequency experiments are more difficult to conduct. Although cracking under viscous deformation has been observed (e.g., Gaye et al. 2014), current laboratory tests do not allow to exhibit a clear fatigue behavior at low frequencies. Moreover, the long-term behavior of salt rock cannot be elucidated with macroscopic laboratory tests and requires an investigation of micro-level processes based on up-scaling or micro-mechanics approaches.

Halite crystal follows a typical face-centered cubic (FCC) structure (Figure 1). Taking all constituents of the crystal as atoms, intra-granular dislocations can occur on planes separating the two densest grain fractions, that is, on planes normal to the $< 1\,1\,1 >$ direction of the grain coordinate system. However, halite crystals comprise two FCC ionic sub-networks (sodium Na^+ and chloride Cl^-). Because of electronic interaction forces between ions, the planes along which sliding requires the minimum energy input are the $\{1\,0\,1\}$ planes.

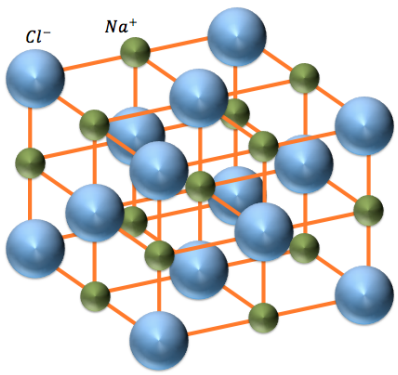

Figure 1: Face-centered cubic (FCC) crystal structure of salt.

In the local coordinate system of the mono-crystal, sliding systems ($\mathbf{A}^l$) are written as

$$\mathbf{A}^l = \mathbf{N}^l \otimes \mathbf{M}^l, \tag{1}$$

in which $\mathbf{N}^l$ is the vector normal to the l^{th} sliding plane and $\mathbf{M}^l$ the l^{th} unit sliding vector, with the sign representing the symmetrized tensor product. The vectors normal to the preferential sliding planes are as follows:

$$\begin{array}{ll} \mathbf{N^1} = \frac{1}{\sqrt{2}}(0,1,1) & \mathbf{N^2} = \frac{1}{\sqrt{2}}(1,0,1) \\ \mathbf{N^3} = \frac{1}{\sqrt{2}}(-1,-1,0) & \mathbf{N^4} = \frac{1}{\sqrt{2}}(0,-1,1) \\ \mathbf{N^5} = \frac{1}{\sqrt{2}}(-1,0,1) & \mathbf{N^6} = \frac{1}{\sqrt{2}}(-1,1,0). \end{array} \tag{2}$$

The sliding directions are given by

$$\begin{array}{lll} \mathbf{M^1} = -\mathbf{N^4} & \mathbf{M^2} = -\mathbf{N^5} & \mathbf{M^3} = -\mathbf{N^6} \\ \mathbf{M^4} = -\mathbf{N^1} & \mathbf{M^5} = -\mathbf{N^2} & \mathbf{M^6} = -\mathbf{N^3} \end{array} \tag{3}$$

Sliding system $\mathbf{N^4} \otimes \mathbf{M^4}$ ($\mathbf{N^5} \otimes \mathbf{M^5}$ and $\mathbf{N^6} \otimes \mathbf{M^6}$, respectively) is normal to sliding system $\mathbf{N^1} \otimes \mathbf{M^1}$ ($\mathbf{N^2} \otimes \mathbf{M^2}$ and $\mathbf{N^3} \otimes \mathbf{M^3}$, respectively). Moreover,

$$\mathbf{N^1} \otimes \mathbf{M^1} = \mathbf{N^2} \otimes \mathbf{M^2} + \mathbf{N^3} \otimes \mathbf{M^3}. \tag{4}$$

Therefore, only two independent sliding mechanisms exist for each grain. In global matrix coordinates, the l^{th} sliding system of the mono-crystal is

$$a^l_{ij} = \frac{n^l_i m^l_j + n^l_j m^l_i}{2}, \tag{5}$$

in which $\boldsymbol{n^l}$ is the vector normal to the l^{th} sliding plane, and $\boldsymbol{m^l}$ is the l^{th} unit sliding vector. Moreover, the viscoplastic deformation of the grain is written as

$$\dot{\varepsilon}^{vp}_{ij} = \sum_{l=1}^{L} \dot{\gamma}^l a^l_{ij}, \tag{6}$$

in which $\dot{\gamma}^l$ is the rate of viscoplastic (shear) deformation of grains subjected to the l^{th} sliding mechanism. For halite mono-crystals, $L = 6$ (with only two independent sliding mechanisms). For each grain, $\left[\mathbf{a}^l\right]$ can be related to the l^{th} sliding mechanism expressed in the local coordinate system, $\left[\mathbf{A}^l\right]$, by means of a projection tensor $[\mathbf{P}]$, which depends on the orientation of the mono crystal:

$$\left[\mathbf{a}^l\right] = [\mathbf{P}] \left[\mathbf{A}^l\right] [\mathbf{P}]^T, \tag{7}$$

where the projection tensor $[\mathbf{P}]$ is decomposed as $[\mathbf{P}] = [\mathbf{P}_1][\mathbf{P}_2][\mathbf{P}_3]$, with

$$[\mathbf{P_1}] = \begin{bmatrix} cos\Psi & sin\Psi & 0 \\ -sin\Psi & cos\Psi & 0 \\ 0 & 0 & 1 \end{bmatrix} \tag{8}$$

$$[\mathbf{P_2}] = \begin{bmatrix} cos\theta & 0 & sin\theta \\ 0 & 1 & 0 \\ -sin\theta & 0 & cos\theta \end{bmatrix} \tag{9}$$

$$[\mathbf{P_3}] = \begin{bmatrix} cos\Phi & -sin\Phi & 0 \\ sin\Phi & cos\Phi & 0 \\ 0 & 0 & 1 \end{bmatrix}, \quad (10)$$

in which Ψ, θ, and Φ are the angles representing the orientation of the grain as described in Section 3.1. Note that contrary to previous salt plasticity models (Pouya 2000), viscoplastic models have no threshold; therefore, sliding mechanisms are all active. Local shear stress (τ^l) is related to micro-stress ($\boldsymbol{\sigma}$) by

$$\tau^l = \boldsymbol{\sigma} : \mathbf{a}^l. \quad (11)$$

Based on the correlations established by Wanten et al. (1996), we assume that the irreversible shear deformation obeys a power law:

$$\dot{\gamma}^l = \gamma_0 \, h^l \left| \frac{\tau^l}{\tau_0} \right|^n, \quad (12)$$

in which n and γ_0 are material parameters, γ_0 a strain rate, and τ_0 a reference shear stress, arbitrarily set equal to 1MPa. In this study, the model is calibrated with γ_0. h^l depends on the sign of τ^l: If τ^l is positive, $h^l = 1$, and if τ^l is negative, $h^l = -1$.

3 HOMOGENIZATION SCHEME

3.1 *Averaging Method*

We consider the representative elementary volume (REV) of salt rock an aggregate of halite mono-crystals of various orientations. Averages computed in the space of crystal orientations form the basis of the upscaling scheme. To determine a system of coordinates in this space, let (X, Y, Z) denote a system of crystallographic axes attached to the inclusion (Figure 2). The orientation of the Z-axis is determined by two spherical coordinates (angles Ψ and θ), defined in the Cartesian coordinate system (x, y, z). Let (u, v, z) be the system obtained from (x, y, z) through rotation around the z-axis at angle Ψ. Let (U, v, Z) be the system obtained from (u, v, z) through rotation around the v-axis at angle θ. System (X, Y, Z) is obtained from system (U, v, Z) by additional "spinal" rotation around the Z-axis at angle Φ, which varies between 0 and 2π.

The probability of having a Z-axis of orientation (Ψ, θ, Φ) is the product of the probability of the occurrence of solid angle Ω (measured by $d\Omega = sin\theta d\theta d\Psi$) by that of spinal rotation Φ (measured by $d\Phi$). Therefore, the density of the probability of the occurrence of grain orientation ω_1 is measured by

$$dp = p(\omega_1)d\omega_1 = p(\Psi, \theta, \Phi)\, sin\theta \, d\theta d\Psi d\Phi. \quad (13)$$

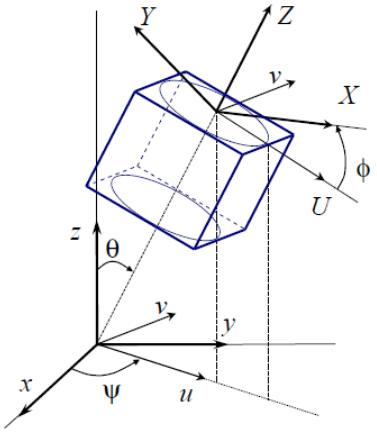

Figure 2: Characterization of mono-crystal orientations in a spherical coordinate system.

The average of a function $f(\omega_1)$ can be defined as

$$\begin{aligned} \overline{f} &= \frac{1}{\Omega_1} \int_{\Omega_1} f(\omega_1) d\omega_1 \\ &= \frac{1}{8\pi^2} \int_{\theta=0}^{\pi} \int_{\Psi=0}^{2\pi} \int_{\Phi=0}^{2\pi} f(\Psi, \theta, \Phi)\, sin\theta \, d\theta d\Psi d\Phi. \end{aligned} \quad (14)$$

Salt rock is made of halite (NaCl) mono-crystals, all of which have the same FCC structure. Since the inclusion (or "grain") represents a single crystal, crystalline symmetries allow the reduction of the variation of Φ to interval $[0, \pi/2]$. Finally, changing θ to $\pi - \theta$, Ψ to $2\pi - \Psi$ and Φ to $2\pi - \Phi$ leads to the same crystallographic orientation (in which Y is replaced by $-Y$). This substitution reduces the domain of variations of θ to interval $[0, \pi/2]$. Because a uniaxial macroscopic loading test is simulated, the REV presents a symmetry around the z-axis. Therefore, Ψ can be set equal to a constant ($\Psi = 0$ is adopted in the following). As a result, in the proposed approach, the average is defined as

$$\overline{f} = \frac{2}{\pi} \int_{\theta=0}^{\pi/2} \int_{\Phi=0}^{\pi/2} f(\theta, \Phi)\, sin\theta \, d\theta d\Phi. \quad (15)$$

Using the variable change $u = cos\theta$, equation (15) can be rewritten as

$$\overline{f} = \frac{2}{\pi} \int_{u=0}^{1} \int_{\Phi=0}^{\pi/2} f(u, \Phi)\, du d\Phi. \quad (16)$$

We assume the same probability of occurrence for all grain orientations, that is, following a uniform probability density function. To obtain equipotent points in a discrete integration scheme, it is sufficient to divide the domain of variation of u ($[0, 1]$) into n_u intervals of central value u_i and the domain of variation of Φ ($[0, \pi/2]$) into n_Φ intervals of central value Φ_j. The average is finally computed as

$$\overline{f} = \frac{1}{N} \sum_{i,j} f(\theta_i, \Phi_j), \quad (17)$$

in which $N = n_u\, n_\Phi$ and $\theta_i = Arcos(u_i)$. We used 200 orientations in the following simulations (i.e., $N = 200$).

3.2 *Inclusion-Matrix Model*

The stresses and strains in mono-crystals depend on the macroscopic load imposed on the aggregate and on the interactions among these mono-crystals. The interactions among grains is accounted for through a simplified "inclusion-matrix model." Following a self-consistent upscaling scheme, each mono-crystal is viewed as an inclusion embedded in an infinite homogeneous matrix that represents the macroscopic aggregate. The behavior of the matrix is *a priori* unknown. Therefore, we apply an upscaling method based on an implicit system of equations: The unknown matrix model has to be determined iteratively. The balance of microscopic stresses at the interface between two constituents is ensured by correcting the macroscopic stress and strain by a so-called *eigenstress* and *eigenstrain*, respectively. REV properties (e.g., the REV stiffness matrix) is deduced from the knowledge of stress and strain concentration tensors, which depend on the geometry of the heterogeneity present in the REV (Nemat-Nasser & Hori 1993, Berryman 1995). We treat mono-crystals as spherical inclusions in the proposed model (Figure 3).

The Kröner model, proposed initially for elasto-plastic materials, was extended by Weng (1982) for viscoplastic materials, in the following form:

$$\dot{\boldsymbol{\sigma}} - \dot{\overline{\boldsymbol{\sigma}}} = 2\mu(1-\beta)(\dot{\overline{\boldsymbol{\varepsilon}}}^{vp} - \dot{\boldsymbol{\varepsilon}}^{vp}), \tag{18}$$

in which $\dot{\boldsymbol{\sigma}}$ is the rate of microscopic stress and $\dot{\overline{\boldsymbol{\sigma}}}$ the rate of macroscopic stress. $\dot{\overline{\boldsymbol{\varepsilon}}}^{vp}$ and $\dot{\boldsymbol{\varepsilon}}^{vp}$ denote the macroscopic and microscopic viscoplastic strain rates, respectively. β is given by

$$\beta = \frac{2(4-5\nu)}{15(1-\nu)}, \tag{19}$$

in which ν is the Poisson's ratio of the homogenized REV (*a priori* unknown).

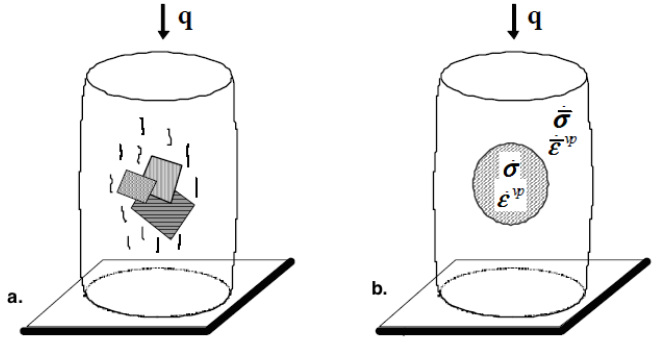

Figure 3: REV of salt rock. a. Monocrystal inclusions in the homogeneous matrix. b. Schematic representation of salt mono-crystals in the inclusion-matrix model.

We consider both the mono-crystal inclusions and the matrix viscoplastic. We adopted the viscoelastic self-consistent model of Weng, which is based on Eshelby's inclusion model. In this model, we assume the matrix-inclusion interaction to be purely elastic, which implies that macroscopic viscoplasticity stems only from grain-scale viscoplastic deformation - not from grain/matrix incompatibilities. Small variations of the local stress in the inclusions ($\boldsymbol{\sigma}$) and small variations of the far-field stress in the matrix ($\overline{\boldsymbol{\sigma}}$) are coupled to variations of the microscopic strain ($\boldsymbol{\varepsilon}$) and variations of the macroscopic strain ($\overline{\boldsymbol{\varepsilon}}$) by the following relationship:

$$\delta\boldsymbol{\sigma} - \delta\overline{\boldsymbol{\sigma}} = -\boldsymbol{L}^* : (\delta\boldsymbol{\varepsilon} - \delta\overline{\boldsymbol{\varepsilon}}), \tag{20}$$

where $\boldsymbol{L}^*$ is Hill's tensor for a spherical inclusion in an isotropic matrix (Hill 1965). This relationship extends equation (18) to a more general case.

3.3 *Micro-macro Damage Modeling*

On the REV scale, we define damage as the reduction of elastic moduli and rock strength. Macroscopically, crack propagation in a rock REV can be driven by tension, compression, or shear (Ortiz 1985, Bobet & Einstein 1998). Although cracks in salt tend to propagate at the interface between grains, we chose to model macroscopic damage as the percentage of grains broken in the REV. Since our approach is based on a matrix-inclusion interaction law, it was easier to update the constitutive relationships of the inclusion than those of the inclusion interfaces. The location of microscopic cracks (inside or between grains) does not influence the computation of the damaged stress and strain fields at the macroscopic level. In brief, we considered that at the grain scale, damage is triggered when one mono-crystal fails. Microscopically, the initiation of damage at the grain scale is restricted to a mode I failure that occurs when the microscopic stress exceeds the tensile strength of salt mono-crystals (equal to 2MPa): If the major principal local stress of a grain exceeds 2 MPa, the grain breaks. Damage propagates when subsequent stress redistribution and further loading bring micro-stress in other grains to the tensile limit. The number of unbroken grains is denoted N_g, the number of broken grains is noted N_b, and the total number of grains in the REV is denoted N (with $N = n_u\, n_\Phi$, the number of mono-crystal orientations in the REV). The dilute scheme estimate for the elastic matrix yields the following effective bulk modulus ($\widetilde{\kappa}$) and shear modulus ($\widetilde{\mu}$):

$$\begin{aligned} \widetilde{\kappa} &= \tfrac{N_g}{N}\kappa = \tfrac{N-N_b}{N}\kappa = (1-D)\kappa \\ \widetilde{\mu} &= \tfrac{N_g}{N}\mu = \tfrac{N-N_b}{N}\mu = (1-D)\mu, \end{aligned} \tag{21}$$

in which the damage variable is defined as $D = N_b/N = 1 - N_g/N$. From the expressions of the damaged bulk and shear moduli in equation (21), we realize that Poisson's ratio does not change upon grain

breakage: $\widetilde{\nu} = \nu$. The proposed micro-macro modeling approach combines Hill's scheme (1965) for the rate-independent non-linear elastic matrix behavior (to represent the inclusion-matrix interaction) and a brittle constitutive law for the grains subject to breakage (to represent damage). We calculate Hill's constraint tensor for the damaged matrix. As a result, in the present work, the inclusion-matrix interaction model accounts for brittle grain breakage, but it does not capture the "viscous accommodation" because of the viscous deformation of the matrix. This simplification is considered acceptable for the sake of this study, which focuses on macroscopic fatigue behavior induced by cyclic loading.

For each macroscopic stress loading increment $\delta q(t)$ applied between times t_n and t_{n+1}, we update the macroscopic and microscopic variables in two steps, as illustrated in figure 4:

1. The "damage phase" ($t_n \sim t_n^+$) accounts for instantaneous variations resulting from grain breakage at time t_n: These variations are denoted $\delta\boldsymbol{\sigma}$, $\delta\boldsymbol{\varepsilon}$, $\delta\overline{\boldsymbol{\sigma}}$, and $\delta\overline{\boldsymbol{\varepsilon}}$.

2. The "viscous phase" ($t_n^+ \sim t_{n+1}$) accounts for time-dependent variations resulting from viscous deformation on the time interval $\Delta_n t = t_{n+1} - t_n$: These variations are denoted $\dot{\sigma}\Delta_n t$, $\dot{\varepsilon}\Delta_n t$, $\dot{\overline{\boldsymbol{\sigma}}}\Delta_n t$, and $\dot{\overline{\boldsymbol{\varepsilon}}}\Delta_n t$.

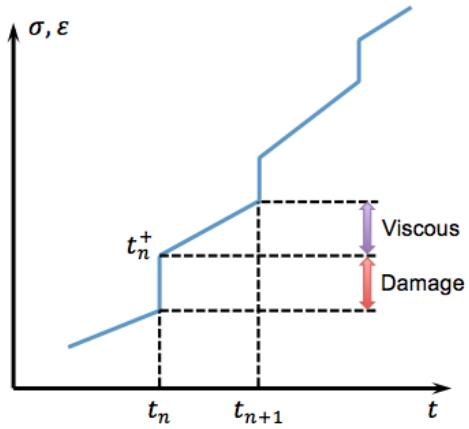

Figure 4: Stress computational method: decomposition of each time step into damage and viscous phases.

At each stress increment (i.e., time step), the grain breakage criterion is checked at the beginning of the damage phase ($t = t_n$). We sort grains into three categories, depending on the stress state of the mono-crystal:

- The grain is non-broken if the maximum principal microscopic stress is less than the mono-crystal tensile strength of 2 MPa.

- The grain is breaking if the maximum principal microscopic stress exceeds the mono-crystal tensile strength of 2 MPa during the current loading increment.

- The grain is broken if the mono-crystal has already been broken in a previous loading increment.

Initially at $t = t_n$, we calculate the damaged elastic moduli from equation (21), in which N_b accounts for both breaking and broken grains. For all types of grains, the inclusion-matrix interaction is governed by Kröner's formula in equation (20). Grain breakage results in a redistribution of micro-stresses: When breaking grains actually fail, non-broken grains become subjected to microscopic stresses of higher magnitude. At the beginning of the viscous phase (at $t = t_n^+$), resulting micro-stresses are updated by equations governing the sliding mechanisms. Note that in some of the grains, the redistribution of micro-stresses resulting from grain breakage (at $t = t_n^+$) can induce tensile stresses that exceed the tensile strength. Grains that are subjected to higher stresses than the tensile strength are considered non-broken during the viscous phase of the loading (between $t = t_n^+$ and $t = t_{n+1}$), and the status of the grains is checked and updated at the beginning of the damage phase of the following loading increment (at $t = t_{n+1}$).

4 MODEL CALIBRATION WITH CREEP TESTS

We determine the model parameters by calibrating the following relationship, which is derived from the basic equations of the micro-macro approach:

$$\dot{p}(t) = \frac{M}{3\mu(1-\beta)} \frac{q^n(t)}{(\tau_0)^n}, \tag{22}$$

in which

$$M = 3\mu(1-\beta)\langle \sum_{l=1}^{L} \gamma_0 \left|\mathbf{r} : \mathbf{a}^l\right|^{n+1} \rangle. \tag{23}$$

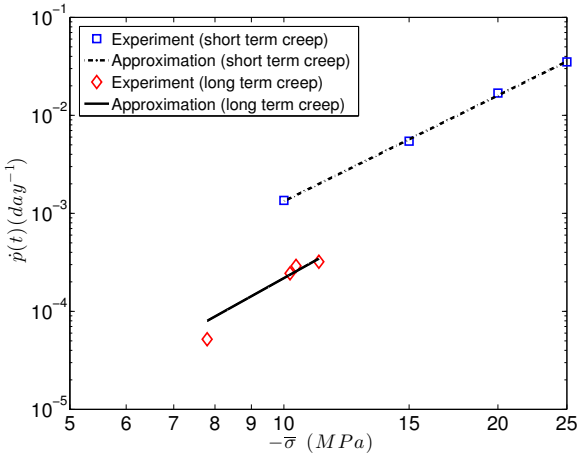

Figure 5: Calibration of the approximated macroscopic creep law against creep tests reported in Fuenkajorn & Phueakphum (2010). Constant loading stress for short-term creep: 10, 15, 20, and 25 MPa. Constant loading stress for long-term creep: 7.8, 10.2, 10.4, and 11.2 MPa.

The relationship in equation (22) directly relates the macroscopic viscoplastic strain rate to the macroscopic stress imposed on the simulations, which allowed us to calibrate the model against experimental data. Note that we made an approximation here: we replaced microscopic stress $\boldsymbol{\sigma}$ by macroscopic stress $\overline{\boldsymbol{\sigma}} = q(t)\mathbf{r}$ in the homogenized equation (11). Details of these derivations are available in Pouya et al. (2014). After calibration, we verified that the variations of macroscopic viscoplastic strains predicted by the approximate law in equation (22) followed those predicted by the non-approximated micro-macro model with less than 5% error.

Table 1: Model parameters calibrated against the creep tests reported in Fuenkajorn & Phueakphum (2010).

Creep Test	γ_0 (day^{-1})	n (-)
Short Term (7 hours)	5.17×10^{-4}	3.58
Long Term (30 days)	2.93×10^{-5}	4.04

Parameter β depends on the macroscopic elastic properties of the polycrystal in the reference state. Poisson's ratio is not affected by damage in the proposed model: A standard value of $\nu_0 = 0.3$ was adopted. The polycrystal Young's modulus is also assigned a value typical of rock salt (Fuenkajorn & Phueakphum 2010): $E_0 = 23GPa$. The microscopic constitutive law in equation (12) depends on two parameters: γ_0 and n. The calibration procedure for γ_0 and n is based on a genetic algorithm that selects an optimal set of parameters that minimizes the difference between the experimental and simulated creep curves. We used short-term (seven hours) and long-term (30 days) creep tests results that are reported in Fuenkajorn & Phueakphum (2010) as reference data. We computed the distance between the reference strain rate and the computed strain rate with the least squares method (Figure 5). The best fit for the two creep tests provided the optimal values of γ_0 and n reported in Table 1. In the simulations that follow, we used the set of parameters calibrated against long-term creep test results.

5 SIMULATIONS OF SALT FATIGUE

5.1 *Salt fatigue under creep loading*

In the following, we present simulations of three long-term creep tests:

- In the first test ("no damage" case), we apply a low creep stress (5.5 MPa) and account for grain breakage.
- In the second test ("non-damage model" case), we apply a high creep stress (6.5 MPa) and ignore grain breakage.
- In the third test ("damage model" case), we apply a high creep stress (6.5 MPa) and account for grain breakage.

We represent the principal values of the microstress of each grain by vector $\sigma_i \overrightarrow{v}_i$, in which the unit vector $\overrightarrow{v}_i$ is the ith microstress eigenvector and σ_i the ith microstress eigenvalue. In plane (r, z), we show a tensile principal stress by vector $\overrightarrow{OM}$ (in the upper right quadrant, $z > 0$, $r > 0$) and a compressive principal stress by vector $\overrightarrow{ON}$ (in the lower left quadrant, $z < 0$, $r < 0$). Figure 6 illustrates the convention adopted to plot microscopic stresses. α measures the angle between the direction of principal microstress and the compression axis z. Stress maps drawn according to the convention explained in Figure 6 show the sign and the amplitude of principal microstresses as well as the angle between principal microstresses and the compression axis for each grain orientation studied in the REV.

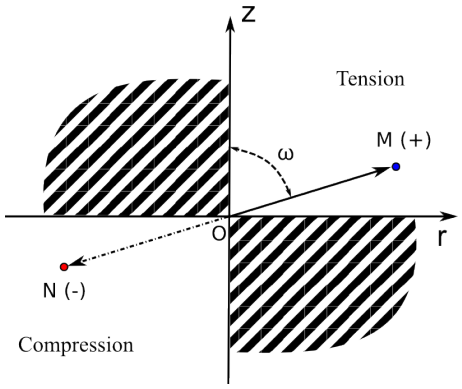

Figure 6: Graphical representation of microscopic principal stresses.

Results are presented in Figure 7:

- In the first test, the macroscopic strain rate reaches a steady state in the secondary creep phase, which indicates an absence of accelerated creep. Microscopic tensile stresses remain below 2 MPa, which implies that none of the monocrystals break even though the model accounts for grain breakage.
- In the second test, the macroscopic strain rate remains almost constant and microscopic stresses exceed the tensile strength limit, which indicates that grains would have been broken if damage had been accounted for.
- In the third test, the microstress goes to zero in 47 grains, and the macroscopic strain rate increases abruptly at the end of the creep test.

These results indicate that the model can capture the accelerated creep regime (tertiary creep) caused by grain breakage. The simulations closely reflect the trends observed in experiments reported by researchers such as Yang et al. (1999) and Fuenkajorn & Phueakphum (2010).

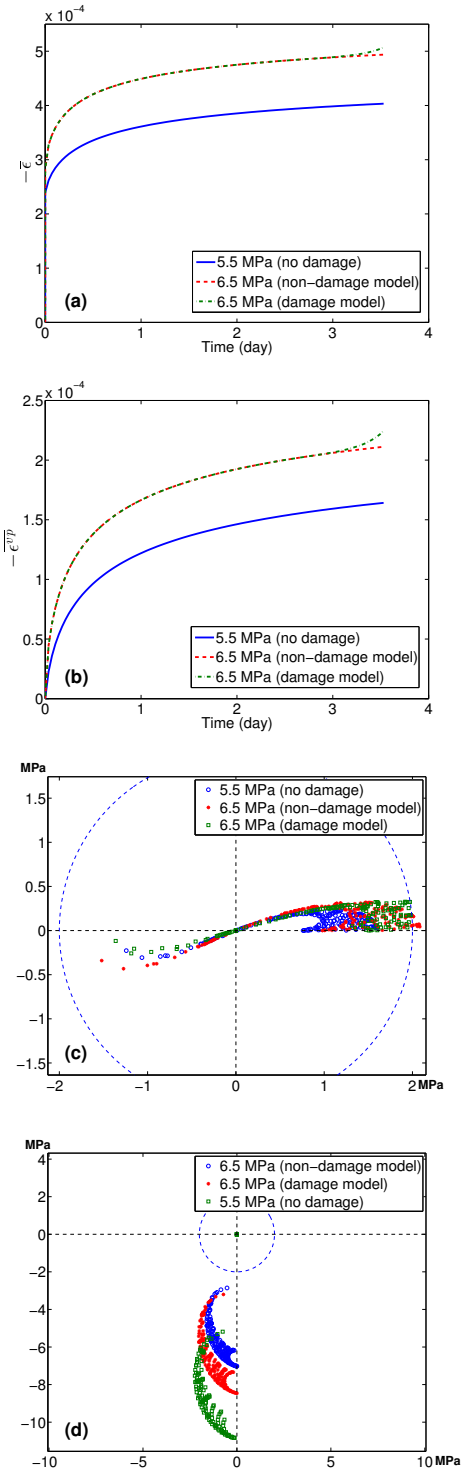

Figure 7: Comparison of different creep tests with and without accounting for grain breakage. (a) Time evolution of total macrostrains. (b) Time evolution of viscoplastic macrostrains. (c) Major microstress component at the end of creep tests. (d) Minor microstress component at the end of creep tests.

5.2 *Salt fatigue under cyclic loading*

The following simulations were performed with the parameters calibrated for the long-term creep behavior ($\gamma_0 = 2.93 \times 10^{-5} day^{-1}$, $n = 4.04$), under loading frequencies typical of CAES conditions. We present three stress-controlled sinusoidal cyclic loading tests:

- In the first test ("non-damage model" case), we apply a cyclic loading with lower frequency 1 day^{-1} and ignore grain breakage.
- In the second test ("non-damage model" case), we apply a cyclic loading with higher frequency 2 day^{-1} and ignore grain breakage.
- In the third test ("damage model" case), we apply a cyclic loading with higher frequency 2 day^{-1} and account for grain breakage.

The maximum stress is 6.5 MPa and the loading amplitude is 2 MPa. We compare the results after 28 cycles. As shown in Figure 8a, different frequencies result in different stress rates. The macroscopic viscoplastic deformation is due to the microscopic viscoplastic strains that develop in the grains: The higher the frequency, the higher the stress rate, and the shorter the time to develop viscoplastic strains. Therefore, for the same final macroscopic stress, higher frequencies induce smaller viscoplastic strains and smaller total strains. Figure 8b shows the subsequent stress-strain curve, similar to the experimental curves reported in Fuenkajorn & Phueakphum (2010) (Figure 7 in particular). The stress-strain cycles tend to a limit behavior, with a constant shifting at each cycle. This limit behavior is analogous to the "adaptation" or "shakedown" effect in elastoplastic media, in which the stress-strain curve exhibits a limit cycle after a large number of loading cycles. Figures 8c and d show the distribution of internal stresses at the end of loading tests. Results confirm that higher frequency leads to smaller microscopic viscoplastic strains, which develop smaller microscopic stresses. Since grain breakage is not accounted for, tensile microscopic stress in some grains exceeds the tensile strength of the monocrystal.

In the third test, when damage is accounted for, failure occurs after a limited number of cycles. The model captures the redistribution of microscopic stresses and presents the results in Figure 8. For minor principal microstresses, some grains experience zero stress as a result of damage. Grain breakage first occurs at the 26^{th} cycle, and the whole polycrystal fails after the 28^{th} cycle. The increasing number of broken grains is visible in the progressive reduction of Young's modulus in the plot of the macroscopic stress/strain curve. Therefore, we note that the model becomes extremely brittle after damage initiation. These results agree with experimental observations reported by Fuenkajorn & Phueakphum (2010), Guo et al. (2012) and Ma et al. (2013). Damage initiates after a low number of cycles. After damage initiation, the behavior becomes extremely brittle: Total failure usually occurs less than five cycles after the initiation of damage.

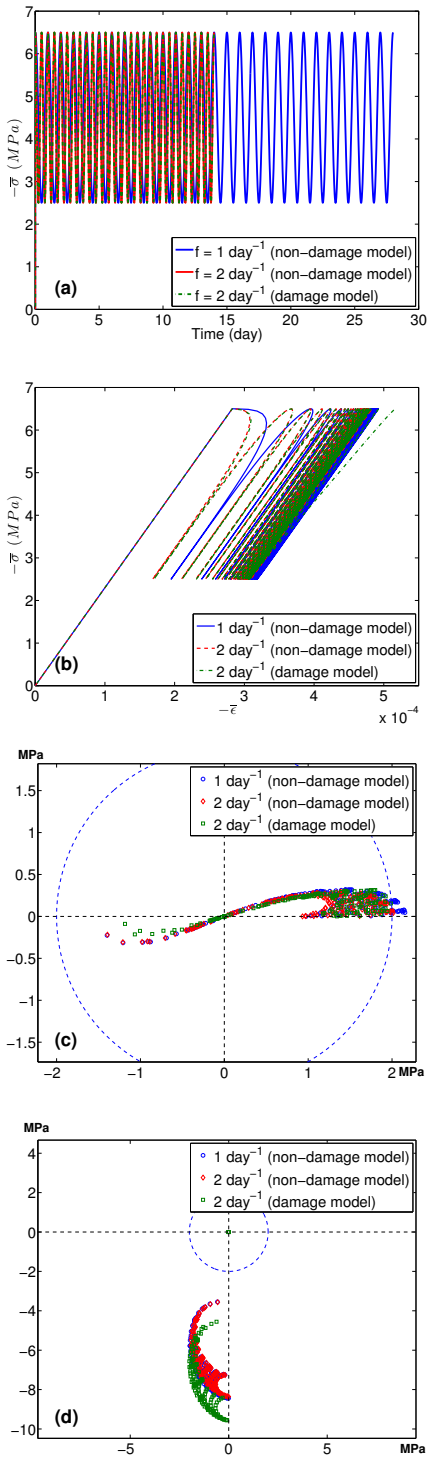

Figure 8: Simulation of cyclic loading tests with a maximum loading stress of 6.5 MPa and an amplitude of 2 MPa.

6 MODEL IMPLEMENTATION IN POROFIS

We implemented our model in a FEM-based program POROFIS (Pouya 2014). This program, written in FORTRAN and using GiD as the pre- and post-processors, enabled us to simulate salt rock behavior with our own creep laws. We modeled a mono-crystal embedded in a homogeneous viscoplastic matrix using POROFIS, and compared the results of creep test simulations obtained from POROFIS to those obtained from the homogenization method above (implemented in MATLAB). The mesh adopted for this model is shown in Figure 9. To describe the behavior of the viscoplastic matrix, we used the approximated macroscopic law in equation (22). The inclusion in the model was circular and modeled with finite elements that were assigned the visco-plastic behavior described by the microscopic constitutive law in equation 12. The grain orientation was assumed to be the same for all elements, so the sphere actually represents one grain. In the following, we present results obtained for $\Psi = 0^o$, $\theta = 39^o$, $\Phi = 43^o$. The size of the grain is small compared to that of the matrix, ensuring the homogeneity of the matrix. Only slip systems number 2 and 5 are active since they lie in the x-z plane, which is the plane of calculation for POROFIS. We adopted a linear viscoelastic law ($n = 1$) and an incompressible matrix ($\nu \approx 0.5$). The creep load was 10 MPa, which was imposed for 1×10^5s ($\sim$1.2 day).

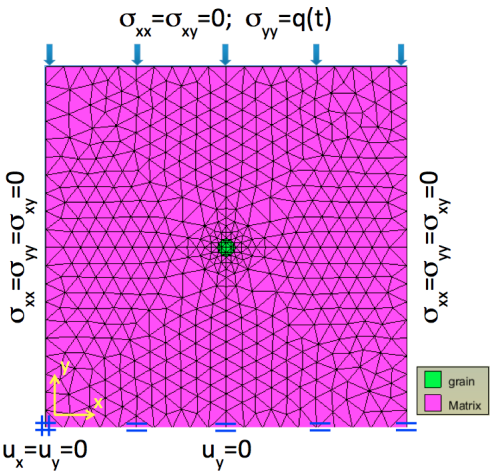

Figure 9: Finite element model in POROFIS

Although we used approximated macroscopic laws in POROFIS and grain incompatibilities are ignored in MATLAB, results from both approaches show close agreement. Figure 10 shows the stress distribution and the matrix deformation at the end of the creep test. Because the grain and the matrix behave differently under the creep load, stress concentrations are observed close to the grain/matrix boundary. We computed the averaged strain of all elements using POROFIS and compared it with the macroscopic strain obtained from the homogenization method with MATLAB (Figure 11). The evolution of strains matches at early stages, but we notice some deviation as time evolves. We retrieved stress values at the integration points of each finite element that represents the grain. We compared the average stress of the grain obtained with POROFIS to the microscopic stress obtained with MATLAB for the same grain orientation. For some orientations, the relative difference was as small as 1.5%, but for a few others, we observed a relative difference of up to 20%. We are currently studying the differences between the MATLAB homogenization model (developed in 3D) and the POROFIS FEM

model (developed in 2D). We will further improve the model to better understand the grain-matrix interaction.

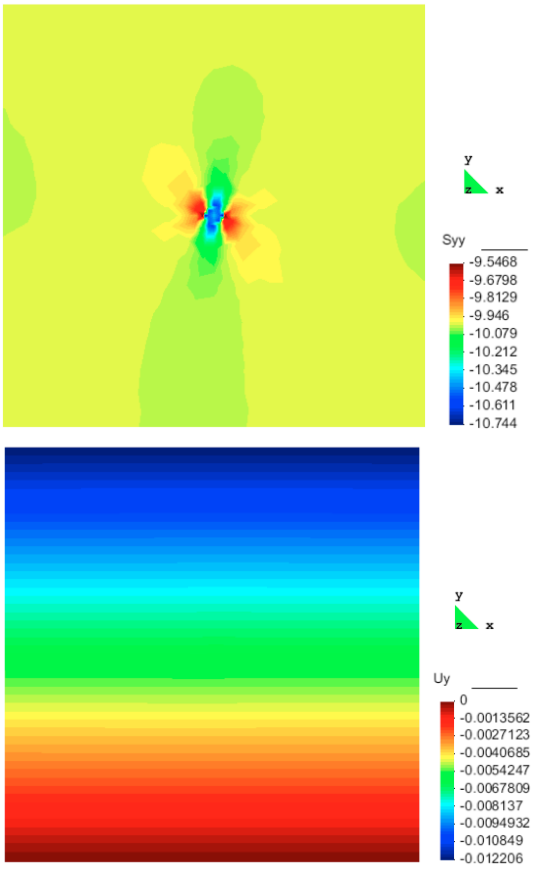

Figure 10: Vertical stress distribution (S_{yy}, in MPa) and vertical displacement (U_y, in m) of the inclusion-matrix model using POROFIS

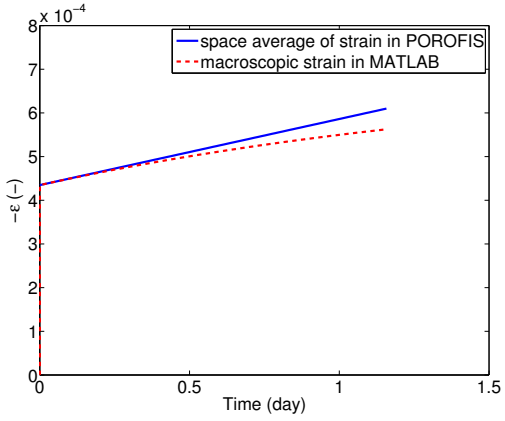

Figure 11: Comparison of strain evolution using POROFIS and MATLAB

7 CONCLUSION

We developed a micro-mechanical model to study the viscous fatigue of salt rock. The representative elementary volume (REV) of salt rock contained monocrystals with a uniform distribution of orientations. The orientation-dependent sliding mechanisms induced viscoplastic deformation at the grain scale. We used an inclusion-matrix model to establish mathematical relationships between microscopic viscoplastic strain and macroscopic viscoplastic strain, and between microscopic stress and macroscopic stress. This model was based on a self-consistent homogenization approach and took grain breakage into consideration. Damage, defined as the ratio of the number of broken grains by the total number of grains, allowed us to predict the progressive loss of stiffness and the strength of the aggregate under cyclic loading.

The proposed micro-macro modeling approach enables the prediction of the viscoplastic-damage behavior of salt rock. We observed strain hardening during creep when the strain rate approached an asymptotic value. As creep loading increased, microscopic stresses increased, resulting in more grain breakage. Grain breakage provided a micro-mechanical interpretation of the phenomenon known as "accelerated creep." For cyclic loading tests, grain breakage occurred at lower frequency and caused the degradation of Young's modulus. The model also captured the dependence of viscoplastic strain on cyclic loading frequency: The higher the frequency, the smaller the macroscopic viscoplastic strain. In addition to the micro-macro computational approach, we implemented governing laws in a finite element program, which was used to model a circular inclusion embedded in a homogeneous matrix. For both computational approaches, macroscopic strains and grain microscopic stresses were similar. Model improvements are still on-going to explain some differences noted in microstresses for certain grain orientations.

Note that the proposed theoretical framework and numerical tools presented herein were not intended to be used for cavern design in their present form. However, the proposed modeling approach advanced our understanding of the microscopic origin of viscous fatigue in salt, which can help provide some guidelines to elaborate relevant macroscopic constitutive models. We will extend our mathematical modeling framework to include geometric incompatibilities between grains and non-elastic inclusion-matrix interactions. We will also improve the damage model by accounting for progressive grain breakage. We will introduce joint elements at the interface between the grain and the matrix in the FEM-based inclusion-matrix model to account for inter-granular geometric incompatibilities.

REFERENCES

Berryman, J.G. 1995. Mixture theories for rock properties. *Rock Physics & Phase Relations: A Handbook of Physical Constants*, 205–228.

Bobet, A. & Einstein, H. 1998. Fracture coalescence in rock-type materials under uniaxial and biaxial compression. *International Journal of Rock Mechanics and Mining Sciences 35*(7), 863–888.

Dubey, R. & Gairola, V. 2000. Influence of structural anisotropy on the uniaxial compressive strength of pre-fatigued rocksalt

from himachal pradesh, india. *International Journal of Rock Mechanics and Mining Sciences 37*(6), 993–999.

Filimonov, Y.L., Lavrov, A., Shafarenko, Y., & Shkuratnik, V. 2001. Memory effects in rock salt under triaxial stress state and their use for stress measurement in a rock mass. *Rock mechanics and rock engineering 34*(4), 275–291.

Fuenkajorn, K. & Phueakphum, D. 2010. Effects of cyclic loading on mechanical properties of maha sarakham salt. *Engineering Geology 112*(1), 43–52.

Gaye, A., Bornert, M., Lenoir, N., Sab, K., Dimanov, A., Bourcier, M., Heripre, E., Raphanel, J., Gharbi, H., Picard, D., & Ludwig, W. 2014. Micromechanics of halite investigated by 2d and 3d multiscale full-field measurements. *48th US Rock Mechanics/Geomechanics Symposium, Minneapolis, 1-4 June.*

Guo, Y.T., Yang, C.H. & Mao, H.J. 2012. Mechanical properties of jintan mine rock salt under complex stress paths. *International Journal of Rock Mechanics and Mining Sciences 56*, 54–61.

Hill, R. 1965. Continuum micro-mechanics of elastoplastic polycrystals. *Journal of the Mechanics and Physics of Solids 13*(2), 89–101.

Liang, W., Zhao, Y., Xu, S. & Dusseault, M. 2011. Effect of strain rate on the mechanical properties of salt rock. *International Journal of Rock Mechanics and Mining Sciences 48*(1), 161–167.

Liu, J.F., Xie, H.P., Hou, Z.M., Yang, C.H. & Chen, L. 2014. Damage evolution of rock salt under cyclic loading in uniaxial tests. *Acta Geotechnica 9*(1), 153–160.

Ma, L.J., Liu, X.Y., Wang, M.Y., Xu, H.F., Hua, R.P., Fan, P.X., Jiang, S.R., Wang, G.A. & Yi, Q.K. 2013. Experimental investigation of the mechanical properties of rock salt under triaxial cyclic loading. *International Journal of Rock Mechanics and Mining Sciences 62*, 34 – 41.

Nemat-Nasser, S. & Hori, M. 1993. Micromechanics: overall properties of heterogeneous solids. *Applied Mathematics and Mechanics. Elsevier, Amsterdam*.

Ortiz, M. 1985. A constitutive theory for the inelastic behavior of concrete. *Mechanics of materials 4*(1), 67–93.

Pouya, A. 2000. Micro-macro approach for the rock salt behaviour. *Eur. J. Mech. A/Solids 19*(6), 1015–1028.

Pouya, A. 2014. A finite element method for modeling coupled flow and deformation in porous fractured media. *International Journal for Numerical and Analytical Methods in Geomechanics (submitted)*.

Pouya, A., Zhu, C. & Arson, C. 2014. Micro-macro approach of salt viscous fatigue under cyclic loading. *Journal of the Mechanics and Physics of Solids (under review)*.

Wanten, P.H., Spiers, C. & Peach, C.J. 1996. Deformation of nacl single crystals at 0.27tm-0.44tm. *Series on Rock and Soil Mechanics 20*, 117–128.

Weng, G. 1982. A unified self-consistent theory for the plastic-creep deformation of metals. *J. Appl. Mech 49*(4), 728–734.

Yang, C., Daemen, J. & Yin, J. 1999. Experimental investigation of creep behavior of salt rock. *International Journal of Rock Mechanics and Mining Sciences 36*(2), 233–242.